

Designing Efficient Energy Funneling Kinetics in Ruddlesden–Popper Perovskites for High-Performance Light-Emitting Diodes

Natalia Yantara, Annalisa Bruno,* Azhar Iqbal, Nur Fadilah Jamaludin, Cesare Soci, Subodh Mhaisalkar, and Nripan Mathews*

Mixed Ruddlesden–Popper (RP) perovskites are of great interest in light-emitting diodes (LEDs), due to the efficient energy transfer (funneling) from high-bandgap (donor) domains to low-bandgap (acceptor) domains, which leads to enhanced photoluminescence (PL) intensity, long PL lifetime, and high-efficiency LEDs. However, the influence of reduced effective emitter centers in the active emissive film, as well as the implications of electrical injection into the larger bandgap donor material, have not been addressed in the context of an active device. The electrical and optical signatures of the energy cascading mechanisms are critically assessed and modulated in a model RP perovskite series $((\text{C}_8\text{H}_{17}\text{NH}_3)_2(\text{CH}(\text{NH}_2)_2)_{m-1}\text{Pb}_m\text{Br}_{3m+1})$. Optimized devices demonstrate a current efficiency of 22.9 cd A^{-1} and 5% external quantum efficiency, more than five times higher than systems where funneling is absent. The signature of nonideal funneling in RP perovskites is revealed by the appearance of donor electroluminescence from the device, followed by a reduction in the LED performance

3D metal halide perovskites (ABX_3 , where A and B are monovalent and divalent cation, respectively, while X is the halide anion) with infinite layers of $[\text{BX}_6]$ octahedral network have demonstrated favorable traits for optoelectronic applications, such as long carrier diffusion lengths,^[1–3] small exciton binding energies,^[4,5] low trap densities,^[6] low recombination rates,^[7] as well as light emission (bandgap) tunability,^[8] and high color

purity.^[9] Organic or inorganic monovalent cations such as methylammonium, formamidinium, and cesium are typically employed for forming the 3D perovskites. The pedigree of perovskite semiconductors are exemplified in the rapid rise in light-emitting diode (LED) efficiencies from $<1\%$ ^[10] to 11.7% ^[11] within 3 years of first reports of light emission. Though slow bimolecular radiative recombination rates found in 3D perovskite are beneficial for photovoltaic application, they fundamentally limit the LED efficiency improvement in which the emitting states need to compete with nonradiative recombination states. As a consequence, high photoluminescence quantum yield (PLQY) and electroluminescence efficiency could only be achieved if the injected carrier densities are higher than the perovskite trap densities. Since the injected current densities during typical LED operation are comparable to 3D perovskite trap densities, strategies to ensure the dominance of bimolecular radiative emission have to be pursued.^[12]

Quasi-2D layered Ruddlesden–Popper (RP, $\text{L}_2\text{A}_{m-1}\text{B}_m\text{X}_{3m+1}$) perovskites have been examined for solar cells to enhance the perovskite moisture resistance through the use of hydrophobic organic molecules.^[13] In this structure, the infinite 3D layers of the $[\text{BX}_6]$ octahedral network are partially separated with high dielectric constant large aliphatic or aromatic alkylammonium layers (L) which act as spacers. For lead halide perovskites ($\text{B} = \text{Pb}$ and $\text{X} = \text{Cl}, \text{Br}, \text{I}$), the conduction and valence band edges of the perovskite rely solely on the orbital contributions from the inorganic octahedron $[\text{PbX}_6]$,^[14] and incorporating 2D cations into the 3D matrix results in a natural multiquantum well system. With multiple bandgap regions present in RP perovskite films, injected carriers are likely to flow from high bandgap “donor” regions to the lower bandgap “acceptor” regions. This results in increased carrier concentrations in the acceptor resulting in enhanced bimolecular radiative rates even at low carrier densities.^[12] Strong carrier concentration has been observed in multidimensional/RP perovskite^[15] with alkyl ammonium,^[16] phenylethylammonium,^[17–20] 1-naphthylmethylammonium,^[11,21,22] and phenylbutylammonium^[23] as the 2D spacer which enhances the luminescence properties of the perovskite films. Despite evidence of energy cascading mechanism through optical characterization, no direct measurements

Dr. N. Yantara, Dr. A. Bruno
Energy Research Institute @ NTU
Nanyang Technological University
Research Techno Plaza, X-Frontier Block, Level 5, 50 Nanyang Drive
637553, Singapore
E-mail: Annalisa@ntu.edu.sg

Dr. A. Iqbal, Prof. C. Soci
Division of Physics and Applied Physics
School of Physical and Mathematical Sciences
Nanyang Technological University
21 Nanyang Link 637371, Singapore

N. F. Jamaludin, Prof. S. Mhaisalkar, Prof. N. Mathews
School of Materials Science and Engineering
Nanyang Technological University
50 Nanyang Avenue 639798, Singapore
E-mail: Nripan@ntu.edu.sg

 The ORCID identification number(s) for the author(s) of this article can be found under <https://doi.org/10.1002/adma.201800818>.

DOI: 10.1002/adma.201800818

utilizing electroluminescence (the key process in LEDs), where the contribution of different components are observable, have been reported. Although energy funneling/cascading increases the radiative recombination through carriers localization, efficiency enhancement in the devices could not be directly attributed to the energy cascading phenomena as other parameters such as light out coupling are also perturbed. The implications of electrical injection from the electron and hole transport layers into the larger bandgap donor material and the optimization of the effective emitter centers have also not been addressed in the context of an active device.

In this work, the importance of cascading was demonstrated through both optical and electrical characterizations by utilizing a $(C_8H_{17}NH_3)_2(CH(NH_2)_2)_{m-1}Pb_mBr_{3m+1}$ RP system. This electrically/optical emissive RP system allows for feedback

from both PL and electroluminescence point of view, enabling an unequivocal comparison. Electrical carrier injection to the donor region was confirmed via the electroluminescence signature that is detected even at turn on voltage of the acceptor poor devices, and energy cascade is verified through charge dynamics as well as device characterization. An optimized system with complete funneling yielded a high-efficiency LED in which current efficiency of 22.9 cd A^{-1} and external quantum efficiency (EQE) of 5% were achieved.

Mixture of 3D formamidinium lead bromide ($CH(NH_2)_2PbBr_3$, Figure 1a) and 2D octylammonium lead bromide ($(C_8H_{17}NH_3)_2PbBr_4$, Figure 1b) perovskite ($\approx 20\%$ 2D) was utilized to form electrically emissive quasi-2D RP ($(C_8H_{17}NH_3)_2(CH(NH_2)_2)_{m-1}Pb_mBr_{3m+1}$) perovskite (Figure 1c). X-ray diffraction (XRD) pattern (Figure S1, Supporting

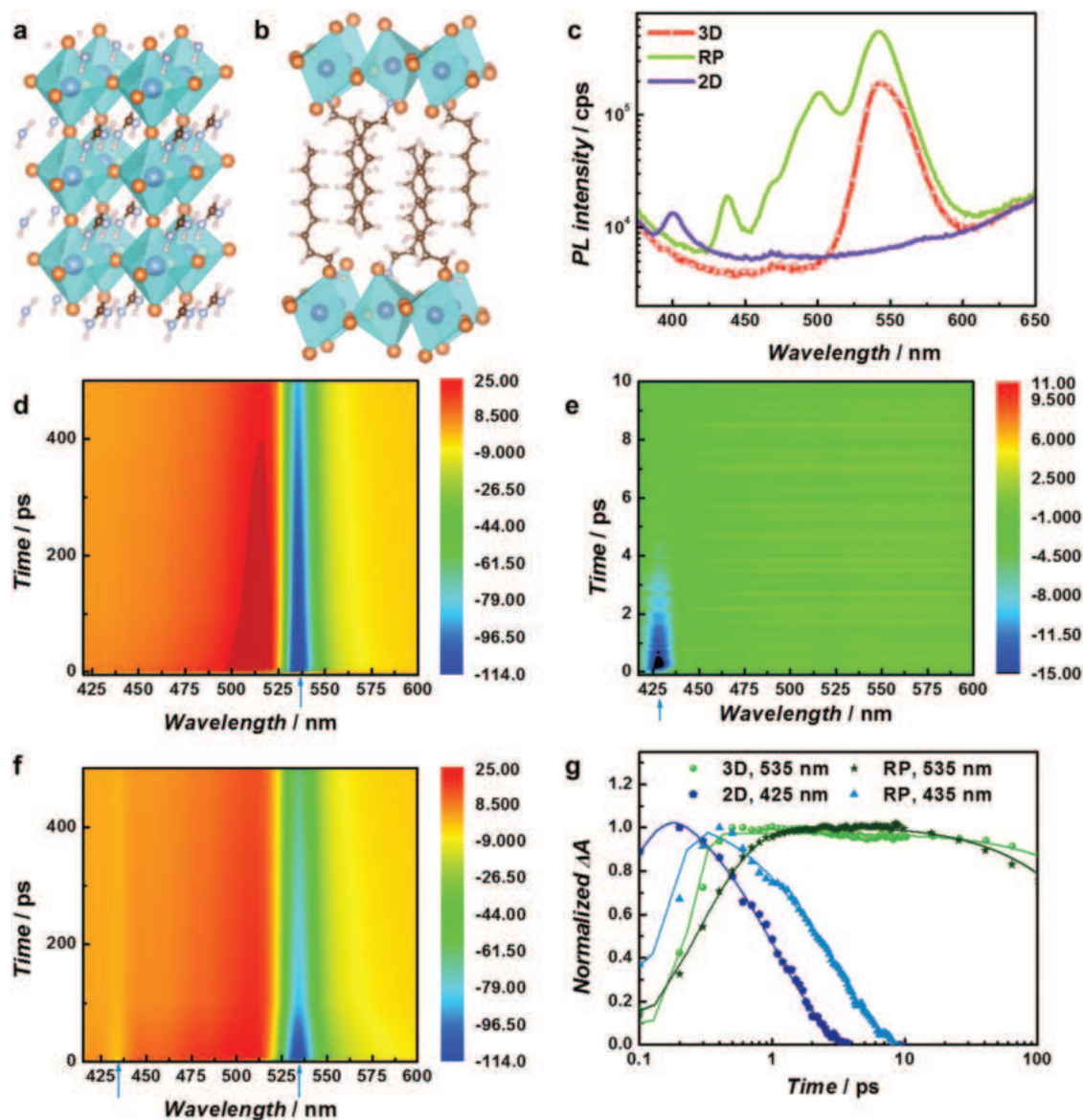


Figure 1. Funneling in RP thin film $(C_8H_{17}NH_3)_2(CH(NH_2)_2)_{m-1}Pb_mBr_{3m+1}$ perovskite. a,b) Schematic crystal structure of 3D $CH(NH_2)_2PbBr_3$ (a) and 2D $(C_8H_{17}NH_3)_2PbBr_4$ (b). c) PL spectra of 3D, 2D, and quasi-2D RP (20% 2D) films. d–g) TA spectra of 3D (d), 2D (e), and quasi-2D RP (f) films at different delay times, as well as the TA kinetics at $\lambda = 425, 435,$ and 535 nm for 2D, RP, and 3D films, respectively (g).

Information) analysis indicates (00) planes interlayer spacing of ≈ 2.1 nm for pure 2D perovskite ($m = 1$, 100%), in agreement with the relationship between alkyl chain length and interlayer spacing ($d(A) = 8.06 + 1.59 \times n$, $n = 8$ for $C_8H_{17}NH_2$) as reported by Takeoka et al.^[24] The XRD spectra of 3D perovskite ($m = \infty$) matched well with the reported value,^[25] while additional peaks at 10° and 13.3° with no 2D diffraction pattern signature were observed on quasi-2D RP film. Formation of multilayered RP phases is deduced as the calculated interlayer spacing for the extra peaks does not add up with the spacing of quasi-2D perovskite assuming $m =$ positive integer.^[24] Steady-state PL peak at 540 and 400 nm were observed for the pure phases of 3D and 2D perovskite, respectively (Figure 1c). On the other hand, multiple PL peaks which do not belong to both 3D and 2D perovskites (Figure 1c) were present on RP films supporting the formation of multilayered RP phases in the samples.

The existence of multilayered RP perovskite phases in the films could potentially drive energy transfer from lower bandgap “donor” domains to higher bandgap “acceptor” domains. Ultrafast transient absorption (TA) spectroscopy (Figure 1d–g) reveals the signature of energy cascade from donor to acceptor material within sub-picosecond (ps) time-scales. Photobleaching signature around 425 and 535 nm was observed for 2D and 3D films, respectively, indicating carrier filling upon excitation above the bandgap (Figure 1d,e). In addition to 535 nm photobleaching peak, traces of carrier filling at 435 nm were also observed for quasi-2D RP samples which corresponded to the multilayered perovskite phase signature (Figure 1f). On the other hand, positive signals (photoinduced absorption) were observed instead for 3D perovskite at 435 nm. The dynamics of photobleaching at 435 and 535 nm peaks are shown in Figure 1g and Table S1 in the Supporting Information, for both 3D and quasi-2D RP samples, respectively. The rise time of 535 nm bleaching signal is about 0.1 ps for 3D film, while a significant slower kinetic was measured at 535 nm (0.39 ps) for RP films. In addition, TA kinetics at 435 nm shows a fast rising time (0.01 ps), indicating instantaneous buildup of excited state followed by fast decay (2.88 ps) for RP samples. These observations clearly demonstrate funneling and prove the accumulation of excited state in 3D phase (photobleaching at 535 nm) that is strongly dominated by the energy transfer from donor (multilayered RP) to acceptor (3D perovskite) domains in RP films.

The efficiency of energy cascading mechanism strongly depends on the overlap between donor PL and acceptor absorption spectra, the distance between acceptor and donor, and the acceptor-to-donor ratio.^[26] Here, the influence of acceptor and donor concentration on the transfer kinetics was scrutinized by varying the concentration of 2D perovskite (i.e., 0–50%) during RP film formation. Multilayered perovskite RP film formation was observed from the XRD spectra (Figure S1, Supporting Information) of all films with traces of 2D perovskite. The intensity of 3D perovskite (0%) diffraction pattern signature, which corresponds to the crystallinity of the film, reduced with increasing 2D concentration, with no diffraction peak signature was observed for 50% 2D samples (i.e., $m = 2$). Pinhole-free films were attained for all samples, as observed in the topographical field-emission scanning electron microscopy (FE-SEM) images (Figure S2, Supporting Information). The

roughness of the films was assessed with atomic force microscope (AFM, Figure S2, Supporting Information), in which additional 10% of 2D resulted in a decrease of the roughness to 5 nm. However, increasing the 2D content above 10% enhances the roughness of the films. Comparable thickness (≈ 300 nm) was observed from the cross-sectional images of both 3D and RP films while grain size reductions were visible with all quasi-2D films. This was caused by the strong electrostatic binding of octylammonium ions on the face of perovskite crystals which subsequently confined grain growth and resulted in grain size reduction.^[27,28] Due to huge grain size variation (20–120 nm) in the film, grain size reduction could not be confirmed in spite of 2D ratio variation.

An optical absorption signature synonymous with a bandgap of 2.36 eV was observed for all films from the steady-state absorption spectra (Figure 2a) fitted using Elliot formula (Figure S3, Supporting Information) attributable to 3D $CH(NH_2)_2PbBr_3$.^[29] The excitonic peak of the 3D perovskite diminished upon addition of 2D perovskite, possibly due to perovskite grain size reduction (Figure 2).^[30] While excitonic signature at ≈ 395 nm was detected for 100% 2D perovskite, additional excitonic peak at 431 nm was detected in quasi-2D films, confirming the formation of multilayered RP perovskite phase, in agreement with the XRD analysis. The 3D absorption signature (i.e., at 529 nm) reduces and the multilayered RP perovskite absorption signature at 431 nm increases with increasing 2D ratio, pointing to a possible bottleneck of reduced low bandgap emission centers.

Steady-state PL intensity was corrected for the number of absorbed photon at the excitation wavelength according to Beer Lambert law and is utilized as a quantitative criterion for comparison. A small Stoke shift between PL and absorption edge was observed, signifying band edge emission of the materials. A single PL peak at 540 nm was detected for 3D and RP films with lower 2D content ($\leq 10\%$). Higher PL intensities were obtained with quasi-2D films as compared with the 3D counterpart with the maximum PL attained with 10% 2D addition. Increasing the 2D ratio above 10% resulted in the appearance of additional broad peaks (resolvable into multiple PL peaks) at smaller wavelength (Figure S4, Supporting Information), indicative of the multilayered RP perovskite structure. Increasing the ratio of 2D above 20% enhances the PL peak intensity at lower wavelength ($\lambda < 540$ nm) and decreases the PL peak at 540 nm. Indication of energy transfer in multilayered RP perovskite is provided by the significant enhancement of 540 nm PL signal for 2D addition up to 20%.

PL excitation spectra (Figure 2b) and time-resolved PL (TRPL) experiments clearly reveal the energy cascading mechanism in all RP films. After excitation at 405 nm, systematic emission wavelength dependent study ($\lambda = 440, 490, \text{ and } 540$ nm) of TRPL reveals energy transfer in the RP film (Figure 2d–f) where slower PL decay kinetics are observed with increasing emission wavelength (Table S2, Supporting Information). Moreover at 540 nm, longer PL lifetimes were observed when RP films were utilized instead of pure 3D perovskite which suggests that energy is cascading to 3D domain which increases the carrier density and subsequently fills in the available trap states. From the PL intensity versus excitation spectra (Figure 2b and Figure S5, Supporting Information), no signature of energy transfer was

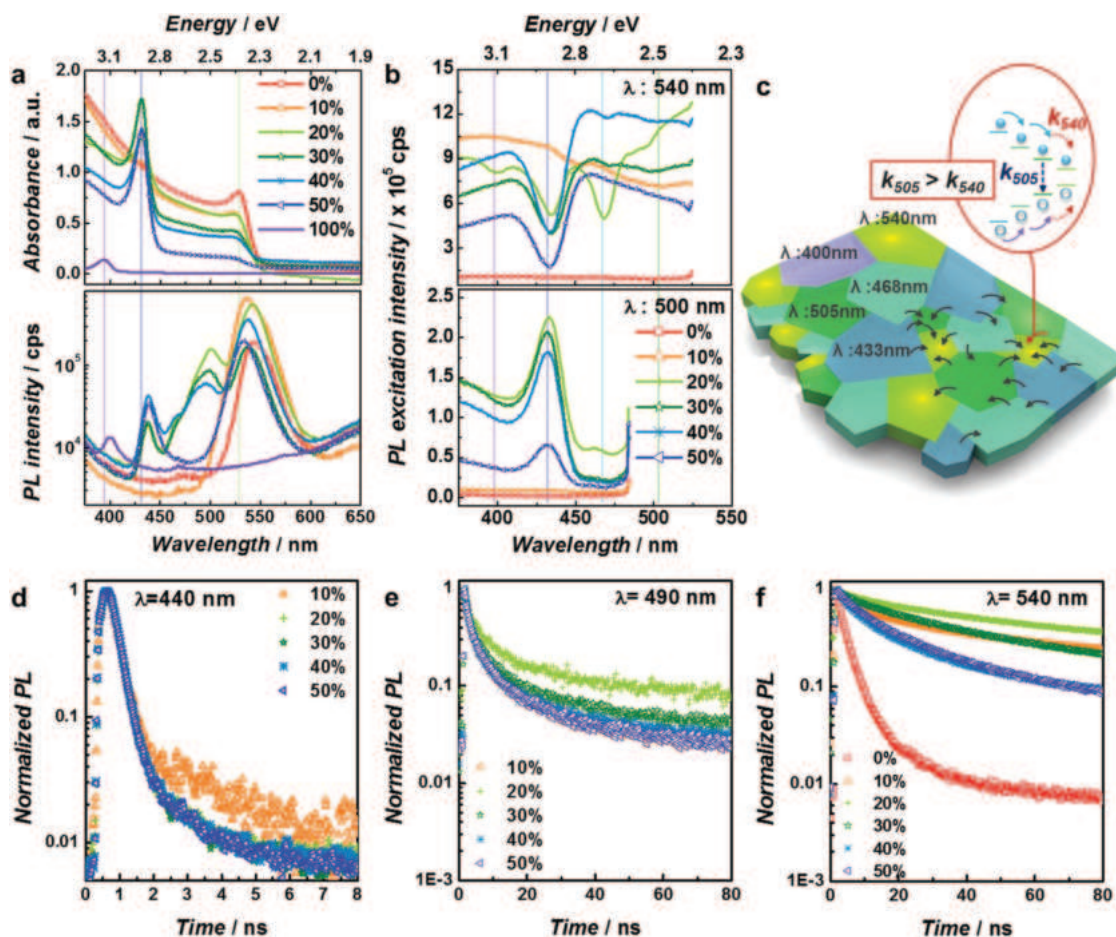


Figure 2. TRPL and PL excitation spectra at various 2D concentrations. a,b) Steady-state absorption and steady-state PL spectra (a) of films followed by the PL excitation spectra at 540 and 500 nm emission (b). c) Schematic diagram of the proposed energy transfer phenomena in the films. d–f) TRPL spectra at 440 (d), 490 (e), and 540 nm (f) emission wavelengths for films at various 2D contents.

visible in 3D perovskite as the PL emission at 500 and 540 nm is independent of excitation wavelengths. On the other hand, multiple peaks were detected on the PL excitation spectra of RP films demonstrating that higher PL emissions were obtained at certain excitation wavelengths. Excitation spectra peaks at 433 and 468 nm were detected when emission was fixed at 500 and 540 nm for 10% 2D film, which confirmed the presence of energy transfer from donor to acceptor.^[11] At higher concentration of 2D perovskite ($\geq 20\%$), depression troughs at 400, 433, and 468 nm excitation wavelengths and a bump at 505 nm excitation wavelength were observed when the emission wavelength was fixed at 540 nm. The depression troughs at 433 and 468 nm became excitation peaks when the emission wavelength was converted to 500 nm. This behavior indicates incomplete energy transfer from 505 nm emitter center (i.e., RP perovskite/donor) to 540 nm emitter center (i.e., 3D perovskite/acceptor) which subsequently resulted in additional steady-state PL peaks (Figure 2a). Although XRD, optical absorption, and steady-state PL spectra indicated no traces of the pure 2D phase, it was detected in the excitation spectra of RP films, indicating that a small amount of $(\text{C}_8\text{H}_{17}\text{NH}_3)_2\text{PbBr}_4$ exists in the film.

Although a graded donor distribution has been proposed to be favorable for efficient energy transfer,^[17] our results

contrarily indicate that the system is still hampered by incomplete energy transfer despite the graded domain noted here as well. Energy transfer from 433 and 468 nm acceptor material occurs while incomplete energy transfer to 540 nm was observed. Energy transfer can occur as radiative transfer, Förster resonance energy transfer, or Dexter transfer. In all cases, the efficiency of energy transfer is related to the donor PL and acceptor absorption spectra overlap, the distance between acceptor and donor, and the acceptor concentration, where higher acceptor concentration would increase the energy transfer efficiency.^[31–33] From the absorption spectra, it is evident that the acceptor concentration decreases with increasing quasi-2D percentage in the film. The average distance between acceptor and donor could also be modulated with varying 2D perovskite concentration. Hence, we postulate that incomplete energy transfer could result from the reduced energy transfer rate (k_{540}) due to low acceptor concentration. The reduction of energy transfer rate could also result in increased recombination (k_{505}) in the donor. The schematic diagram of the proposed mechanism is presented in Figure 2c.

To validate the importance of efficient electrical energy cascade behavior, light-emitting device stacks were fabricated with lithium fluoride (LiF) and ((1,3,5-triazine-2,4,6-triyl)

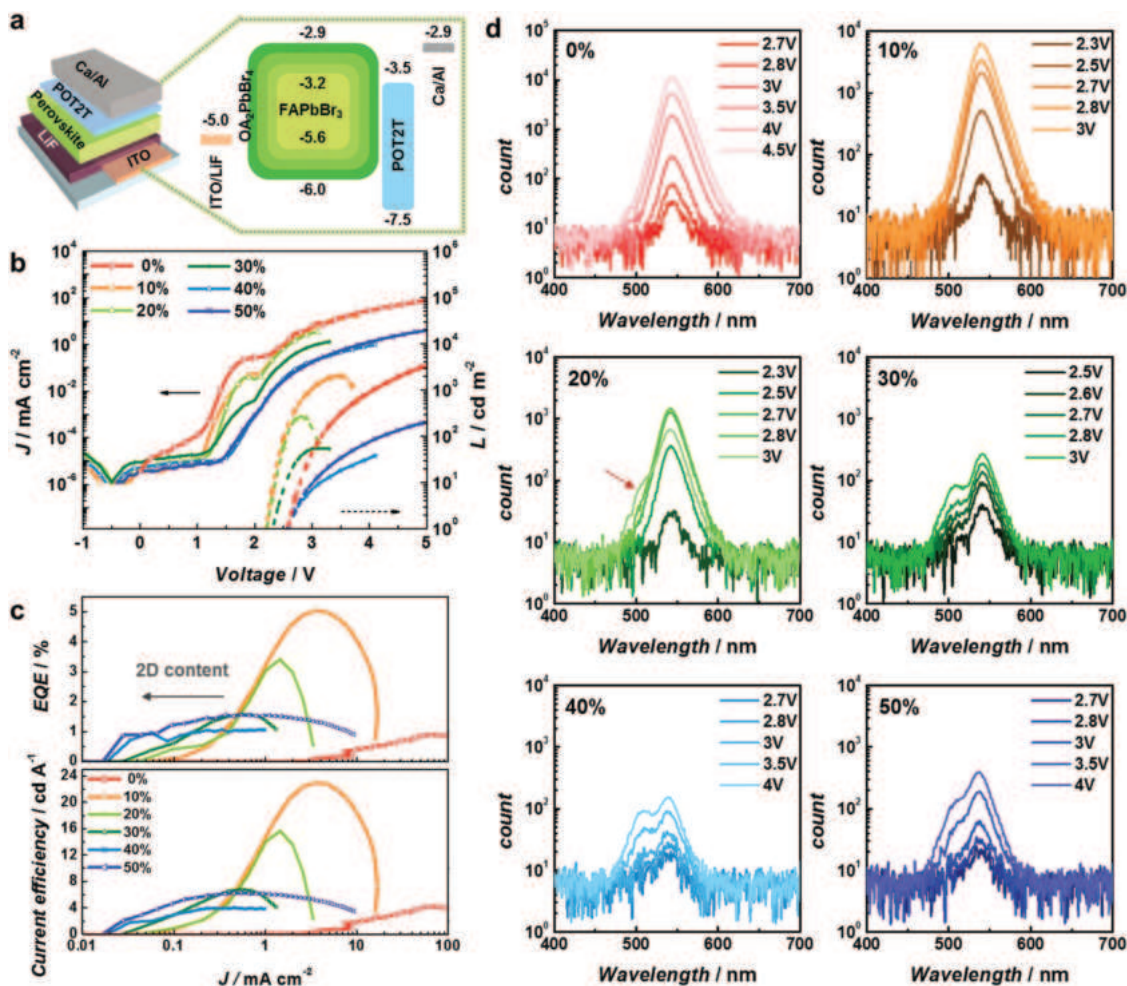


Figure 3. Device performances and electroluminescence (EL) spectra of RP perovskite. a–d) Band diagram of the LED devices (a) followed by the corresponding J – V – L curve (b), EQE and current efficiency curve (c), as well as the electroluminescence spectra (d) of all devices at various bias applications.

tris(benzene-3,1-diyl)tris(diphenylphosphine oxide) (POT2T) as hole-transporting layer (HTL) and electron-transporting layer, (ETL) respectively. The band energy alignment employed in the devices was presented in Figure 3a. The current density–voltage–luminance (J – V – L) characteristics as well as the EQE, current efficiency, and electroluminescence spectra were presented in Figure 3. From J – V curves, reduction of the carrier injection to emitter is visible with increasing multilayered RP concentration as the current turn on voltages (V_{on} , voltage at which $J \approx V^m$) shifted toward higher bias for comparable leakage currents (current at which $J \approx V$, Figure 3b). Efficient carrier injection was observed in the device with higher acceptor content ($\leq 20\%$ 2D) as subbandgap light turn on voltage (V_{th} , voltage at 1 cd m^{-2}) $\approx 2.2 \text{ V}$ was observed. Higher V_{th} indicates that carrier injection rate to the emitter is slightly reduced especially when higher donor content ($>20\%$ 2D) was employed.

The maximum current efficiency and EQE of the pure 3D devices were 4.17 cd A^{-1} , and 0.89% respectively. Employing RP films enhance the current efficiency, and EQE by at least 1 order of magnitude depending on the 2D ratio used (Figure 3c). A maximum current efficiency of 22.9 cd A^{-1} and EQE of 5% were achieved with 10% 2D films (Figure 3c). Enhancing the

2D ratio above 10% resulted in an efficiency drop to approximately half of the EQE obtained with 10% 2D. Higher 2D ratios resulted in greater efficiency at low J regime, consistent with energy cascading resulting in high PLQY at lower power density due to strong carrier concentration at the effective emitter acceptor material.^[12,17] Similar observations were also observed when different ETL (i.e., 2,2',2''-(1,3,5-benzinetriyl)-tris(1-phenyl-1-*H*-benzimidazole) – TPBi) and HTL (i.e., poly(3,4-ethylenedioxythiophene) polystyrene sulfonate – Pedot:PSS) with lower injection efficiency (i.e., higher V_{th}) to the emitter were used (Figure S6, Supporting Information).

The electroluminescence spectra of the devices were taken at various bias applications (Figure 3d). Electroluminescence peak at 540 nm was observed for pure 3D devices, in agreement with the PL peak of the film. When high acceptor concentration was employed (10% 2D), a single electroluminescence peak was observed at 540 nm regardless of the bias application. With 20% 2D addition, a concurrent presence of the extra donor electroluminescence peak at 505 nm and an efficiency drop were observed for bias application larger than 2.7 V . The consistency between the appearance of the extra donor electroluminescence peak and efficiency drop in the same device rules out

light out coupling as a source of variation. This indicates that incomplete energy transfer resulted in low device efficiency, as expected from the optical measurements. Similar to quantum dot based LED, wider carrier generation region at higher currents simultaneously extending distance between donor and acceptor, which could lead to decrease of energy cascade rate and increase probability of donor radiative recombination.^[34] Increasing the current further resulted in significant increase of carrier concentration at the acceptor, which could lead to Auger recombination facilitated quenching of the acceptor emission.^[34]

The presence of extra donor electroluminescence peak at 505 nm for RP device with lower acceptor concentration (>20% 2D) even at V_{th} (≈ 2.5 V) signifies the capability of the employed ETL and HTL to electrically inject carriers to donor material. As the acceptor concentration is decreased with increasing 2D ratio (>20%), the energy cascade rate is reduced resulting in high probability of donor radiative emission as evidenced by the appearance of the donor's 505 nm electroluminescence peak. Therefore, it is evident that complete energy cascading behavior is a key factor to gain high-efficiency light-emitting devices. To the best of our knowledge, we report the first direct evidence of energy cascading in electrical characterization of RP perovskite based LED. The carrier injection to wide bandgap donor material is illustrated together with the importance of well-engineered donor and acceptor regions ratio to device efficiency. While other factors such as surface roughness and crystallite size of the films would modulate the efficiency of LED devices to a certain extent, we have isolated them to identify the impact of energy transfer within the phases in the film on the LED performances here (Figure S7, Supporting Information).

By using electrically emissive $(C_8H_{17}NH_3)_2(CH(NH_2)_2)_{m-1}Pb_mBr_{3m+1}$ RP materials, the importance of energy funneling for LED application was presented through optical and electrical characterization. The appearance of extra electroluminescence signature from donor domains even at lower voltage indicates the possibility of carrier injection to the donor domains. It is apparent that energy cascading mechanism could increase the local carrier density which resulted in higher LED efficiency at low carrier injection regime. When the acceptor-to-donor concentration ratio is low, the rate of the energy transfer becomes slower which resulted in inefficient energy transfer. Subsequently, we successfully identified both PL and electroluminescence signatures of high bandgap RP material and a concurrent drop in both the acceptor PL intensity and LED efficiency. Therefore, a well-engineered acceptor-to-donor ratio, which could be varied by changing the precursors, is essential to create pathways for high-efficiency LED. System with efficient cascading behavior resulted in high-efficiency LED at which 5% EQE and 22.9 cd A⁻¹ current efficiency were realized.

Experimental Section

Perovskite Film Formation: Mixture of equimolar (1 M) $CH(NH_2)_2Br$ and $PbBr_2$ in DMF:DMSO (75:25) solvent was used to produce pure 3D perovskite. Pure 2D perovskite solution was synthesized with $C_8H_{17}NH_3Br$ (2 M) and $PbBr_2$ (1 M) in DMF:DMSO (75:25 by volume) solvent. Quasi-2D solutions were produced by mixing both pure 3D

and pure 2D perovskite solutions in different ratios (i.e., from 0% 2D to 50% 2D). Films were then fabricated by spin coating from various perovskite solutions where antisolvent (i.e., toluene) was used to enhance the coverage of the resulting film. The films were then dried in room temperature. Both spin coating and solution mixing were done under argon environment.

Device Fabrication: Indium tin oxide (ITO) coated glass was used as the substrates. Depending on the choice of ETL and HTL, two types of devices were used. In Device A, poly(3,4-ethylenedioxythiophene) polystyrene sulfonate (Pedot:PSS, Al 4083) was spun coated on top of ITO at 4000 rpm for 1 min followed by heating at 150 °C for 10 min. Substrates were then transported inside glovebox for perovskite deposition. Approximately, 40 nm of TPBi was thermally evaporated. For Device B, 0.5 nm of LiF was thermally evaporated to replace Pedot:PSS, while 40 nm of POT2T was thermally evaporated instead of TPBi. Devices were then completed by thermal evaporation of the electrode (i.e., 10 nm of calcium and 100 nm of aluminum). Device area was fixed at 8 mm² by using shadow mask during electrode evaporation.

Physical Characterization: The crystallographic information of the films was assessed using Bruker D8 advance diffractometer with OD LynxEYETM detector. The scans were conducted on perovskite film deposited on top of Pedot:PSS coated glass substrates. (FE-SEM, JEOL J7600F) was employed to capture the topographical and cross-sectional images. AFM (Asylum Research MFP-3D) with contact modes were used with Ti/Ir coated cantilevers (ASYLEEC-01-R2, Asylum Research) for surface roughness measurement. Shimadzu UV-3600 UV-vis-NIR spectrophotometer was used to collect the absorption spectra while Horiba Fluoromax-4 was utilized to obtain the steady-state PL spectra as well as the excitation spectra.

TRPL dynamics were collected using micro-PL setup, employing a Nikon microscope, and using a Picoquant PicoHarp 300 time-correlated single photon counting (TCSPC) system. The excitation source is a ps pulsed laser diode (Picoquant P-C-405B, $\lambda = 405$ nm, 40 MHz repetition rate). Output signal was processed through Acton SP-2300i monochromator for spectral selection of the emission light coupled to an avalanche diode synchronized with excitation laser via TCSPC electronic. Overall, the full width at half maximum of the system instrument respond function is around 50 ps.

A home-built femtosecond pump-probe setup was used to conduct the TA measurements. A commercial amplifier, Quantronix Integra-C, was externally seeded by a mode-locked Ti:Sapphire oscillator (Ti-Light) that delivered >200 mW average power up to 100 nm bandwidth. The pulse energy of nJ was amplified to a level of few mJ. The amplifier operated at a repetition rate of 1 kHz with pulse duration of 100 fs. Briefly, the fundamental 800 nm output pulse was split in two beams with a beam splitter. One beam was used to pump the optical parametric amplifier and second beam was used to generate pump and probe pulses by using a beam splitter. A pump wavelength of 400 nm was generated by frequency doubling using the type-I BBO crystal. A probe beam of broadband white light with a highest cutoff wavelength 350 nm (3.54 eV) was generated by using 3 mm thick calcium fluoride (CaF_2) crystal via white light continuum generation. In order to avoid the laser induced damage, the crystal was continuously spun during the measurements. The delay between the pump and probe pulses was controlled by motorized delay stage. The pump pulses were chopped at 500 Hz by a synchronized chopper, and the absorbance changes were calculated with two adjacent probe pulses, i.e., pump blocked and pump unblocked. Commercial spectrometer, Jobin Yvon CP140 – 104, coupled with a silicon photodiode array was used to record TA spectra (Entwicklungsbüro Stresing). A shortwave pass filter was used to cut off the low energy end of the white light spectrum at 1.77 eV (700 nm) in order to remove higher diffraction orders artifacts in the measurements. To overcome the problem of white light instability artifacts in the measured TA spectra, selected spectra at different time delays were obtained for 100 measurement cycles at an exposure time of 100 ms. Experiments were conducted at room temperature and samples were kept in nitrogen environment.

Device Characterization: A Keithley 2612B was employed to measure the current–voltage response of the devices. The forward-emission light output was collected by placing the device outside and facing into the opening of an integrating sphere (OceanOptics FOIS-1) connected to a calibrated spectrometer (OceanOptics QEPro). An Ocean Optics HL-3 Plus vis–NIR light source, which was calibrated using a process and documentation based on ISO 17 025, IEC Guide 115, and JCGM100:2008 (GUM) protocols, was used to calibrate the absolute irradiance.

Supporting Information

Supporting Information is available from the Wiley Online Library.

Acknowledgements

This research was funded by National Research Foundation, Prime Minister's Office, Singapore under its Competitive Research Programme (CRP Award No. NRF-CRP14-2014-03) and Singapore–Berkeley Research Initiative for Sustainable Energy (SinBeRISE) CREATE Program.

Conflict of Interest

The authors declare no conflict of interest.

Keywords

electroluminescence, funneling, halide perovskites, light-emitting diodes, Ruddlesden–Popper

Received: February 5, 2018

Revised: May 17, 2018

Published online:

- [1] G. Xing, N. Mathews, S. Sun, S. S. Lim, Y. M. Lam, M. Grätzel, S. Mhaisalkar, T. C. Sum, *Science* **2013**, *342*, 344.
- [2] E. Edri, S. Kirmayer, S. Mukhopadhyay, K. Gartsman, G. Hodes, D. Cahen, *Nat. Commun.* **2014**, *5*, 3461.
- [3] S. D. Stranks, G. E. Eperon, G. Grancini, C. Menelaou, M. J. P. Alcocer, T. Leijtens, L. M. Herz, A. Petrozza, H. J. Snaith, *Science* **2013**, *342*, 341.
- [4] T. Ishihara, *J. Lumin.* **1994**, *61*, 269.
- [5] S. Sun, T. Salim, N. Mathews, M. Duchamp, C. Boothroyd, G. Xing, T. C. Sum, Y. M. Lam, *Energy Environ. Sci.* **2014**, *7*, 399.
- [6] G. Xing, N. Mathews, S. S. Lim, N. Yantara, X. Liu, D. Sabba, M. Grätzel, S. Mhaisalkar, T. C. Sum, *Nat. Mater.* **2014**, *13*, 476.
- [7] C. Wehrenfennig, G. E. Eperon, M. B. Johnston, H. J. Snaith, L. M. Herz, *Adv. Mater.* **2014**, *26*, 1584.
- [8] J. H. Noh, S. H. Im, J. H. Heo, T. N. Mandal, S. I. Seok, *Nano Lett.* **2013**, *13*, 1764.
- [9] S. Adjokatse, H. H. Fang, M. A. Loi, *Mater. Today* **2017**, *20*, 413.
- [10] Z.-K. Tan, R. S. Moghaddam, M. L. Lai, P. Docampo, R. Higler, F. Deschler, M. Price, A. Sadhanala, L. M. Pazos, D. Credgington, F. Hanusch, T. Bein, H. J. Snaith, R. H. Friend, *Nat. Nanotechnol.* **2014**, *9*, 687.
- [11] N. Wang, L. Cheng, R. Ge, S. Zhang, Y. Miao, W. Zou, C. Yi, Y. Sun, Y. Cao, R. Yang, Y. Wei, Q. Guo, Y. Ke, M. Yu, Y. Jin, Y. Liu, Q. Ding, D. Di, L. Yang, G. Xing, H. Tian, C. Jin, F. Gao, R. H. Friend, J. Wang, W. Huang, *Nat. Photonics* **2016**, *10*, 699.
- [12] G. Xing, B. Wu, X. Wu, M. Li, B. Du, Q. Wei, J. Guo, E. K. L. Yeow, T. C. Sum, W. Huang, *Nat. Commun.* **2017**, *8*, 14558.
- [13] I. C. Smith, E. T. Hoke, D. Solis-Ibarra, M. D. McGehee, H. I. Karunadasa, *Angew. Chem., Int. Ed.* **2014**, *53*, 11232.
- [14] J. Endres, D. A. Egger, M. Kulbak, R. A. Kerner, L. Zhao, S. H. Silver, G. Hodes, B. P. Rand, D. Cahen, L. Kronik, A. Kahn, *J. Phys. Chem. Lett.* **2016**, *7*, 2722.
- [15] T. M. Koh, K. Thirumal, H. Sen Soo, N. Mathews, *ChemSusChem* **2016**, *9*, 2541.
- [16] X. Y. Chin, A. Perumal, A. Bruno, N. Yantara, S. Veldhuis, L. Martinez-Sarti, B. Chandran, V. S. Chirvony, S.-Z. A. Lo, J. So, C. Soci, M. Grätzel, H. J. Bolink, N. Mathews, S. G. Mhaisalkar, *Energy Environ. Sci.* **2018**, <https://doi.org/10.1039/C8EE00293B>.
- [17] L. N. Quan, Y. Zhao, F. P. García De Arquer, R. Sabatini, G. Walters, O. Voznyy, R. Comin, Y. Li, J. Z. Fan, H. Tan, J. Pan, M. Yuan, O. M. Bakr, Z. Lu, D. H. Kim, E. H. Sargent, *Nano Lett.* **2017**, *17*, 3701.
- [18] M. Yuan, L. N. Quan, R. Comin, G. Walters, R. Sabatini, O. Voznyy, S. Hoogland, Y. Zhao, E. M. Bearegard, P. Kanjanaboos, Z. Lu, D. H. Kim, E. H. Sargent, *Nat. Nanotechnol.* **2016**, *11*, 872.
- [19] Y. F. Ng, S. A. Kulkarni, S. Parida, N. F. Jamaludin, N. Yantara, A. Bruno, C. Soci, S. G. Mhaisalkar, N. Mathews, *Chem. Commun.* **2017**, *53*, <https://doi.org/10.1039/C7CC06615E>.
- [20] X. Yang, X. Zhang, J. Deng, Z. Chu, Q. Jiang, J. Meng, P. Wang, L. Zhang, Z. Yin, J. You, *Nat. Commun.* **2018**, *9*, 2.
- [21] S. Zhang, C. Yi, N. Wang, Y. Sun, W. Zou, Y. Wei, Y. Cao, Y. Miao, R. Li, Y. Yin, N. Zhao, J. Wang, W. Huang, *Adv. Mater.* **2017**, *29*, 1.
- [22] W. Zou, R. Li, S. Zhang, Y. Liu, N. Wang, Y. Cao, Y. Miao, M. Xu, Q. Guo, D. Di, L. Zhang, C. Yi, F. Gao, R. H. Friend, J. Wang, W. Huang, *Nat. Commun.* **2018**, *9*, 608.
- [23] J. Si, Y. Liu, Z. He, H. Du, K. Du, D. Chen, J. Li, M. Xu, H. Tian, H. He, D. Di, C. Lin, Y. Cheng, J. Wang, Y. Jin, *ACS Nano* **2017**, *11*, 11100.
- [24] Y. Takeoka, K. Asai, M. Rikukawa, K. Sanui, *Bull. Chem. Soc. Jpn.* **2006**, *79*, 1607.
- [25] G. E. Eperon, S. D. Stranks, C. Menelaou, M. B. Johnston, L. M. Herz, H. J. Snaith, *Energy Environ. Sci.* **2014**, *7*, 982.
- [26] J. R. Lakowicz, *Principles of Fluorescence Spectroscopy*, Springer, New York, USA **2006**.
- [27] Y. Chen, Y. Sun, J. Peng, J. Tang, K. Zheng, Z. Liang, *Adv. Mater.* **2017**, *17*, 1703487.
- [28] S. A. Kulkarni, S. Muduli, G. Xing, N. Yantara, M. Li, S. Chen, T. C. Sum, N. Mathews, T. J. White, S. G. Mhaisalkar, *ChemSusChem* **2017**, *10*, 3818.
- [29] S. Chen, A. Nurmikko, *ACS Photonics* **2017**, *4*, 2486.
- [30] A. R. Srimath Kandada, A. Petrozza, *Acc. Chem. Res.* **2016**, *49*, 536.
- [31] C. B. Murphy, Y. Zhang, T. Troxler, V. Ferry, J. J. Martin, W. E. Jones, *J. Phys. Chem. B* **2004**, *108*, 1537.
- [32] A. Govorov, P. L. H. Martínez, H. V. Demir, in *Underst. Model. FRET Förster-Type Reson. Energy Transf. Introd. to Förster-Type Reson. Energy Transf.*, **2016**, pp. 14–15.
- [33] J. B. Hoffman, R. Alam, P. V. Kamat, *ACS Energy Lett.* **2017**, *2*, 391.
- [34] P. O. Anikeeva, C. F. Madigan, J. E. Halpert, M. G. Bawendi, V. Bulović, *Phys. Rev. B* **2008**, *78*, 85434.